International Forum on Aeroelasticity and Structural Dynamics
IFASD 2024
17-21 June 2024, The Hague, The Netherlands

DESIGN, MANUFACTURING AND IDENTIFICATION OF AN ACTIVELY CONTROLLED FLEXIBLE WING FOR SUBSONIC WIND TUNNEL TESTING

Johannes Dillinger[1], Holger Mai[1], Wolf R. Krüger[1], Thomas G. Schmidt[1], Felix Stalla[2]

[1]DLR - Institute of Aeroelasticity
Bunsenstrasse 10, 37073 Göttingen, Germany
Johannes.Dillinger@dlr.de
Holger.Mai@dlr.de
Wolf.Krueger@dlr.de
TG.Schmidt@dlr.de

[2]DLR - Institute of System Dynamics and Control
Münchener Strasse 20, 82234 Wessling, Germany
felix.stalla@dlr.de

Keywords: aeroservoelasticity, wind tunnel testing, comsposite optimization

Abstract: To minimize the climate impact of commercial flight, aircraft emissions have to be significantly reduced. Important contributions towards this goal are the reduction both of aircraft drag and of structural mass. An increase of wing aspect ratio is a well-known design measure to reduce induced drag, however, a higher wing span usually leads to higher wing mass because of increased structural loads. Thus, load alleviation is essential for the realization of high aspect ratio wings, active gust load alleviation being a promising step to further decrease sizing loads. The paper presents the design, manufacturing and testing of an actively controlled wing in the *German Aerospace Center* (DLR) project *oLAF* (optimized load adaptive wing). A wing of $1.75\,m$ semi-span is designed and built, equipped with five trailing edge devices (flaperons/ailerons) and two spoilers. The sensors built into in the wing include 12 accelerometers, 10 pressure sensors and a fiber-optical sensor for strain measurements. Furthermore, the forces and moments of a piezo-balance in the wind tunnel mounting are available for feedback, and a marker-based optical measurement system is used for the high-speed tracking of wing and control surface deflections. The wind tunnel campaign takes place at the DNW-NWB subsonic wind tunnel in Braunschweig, a tunnel belonging to the German and Dutch Wind Tunnel organization. The wind tunnel has a cross section of $3.25\,m$ x $2.8\,m$ and is operating at a maximum flow speed of $90\,m/s$. For the experiment, a gust generator is specifically designed, based on four stationary airfoil vanes, each followed by a downstream rotating, slotted cylinder (RSC) mounted vertically. Load control is implemented on a real-time environment based on control laws being developed in MATLAB/Simulink. The design of the wing, as well as that of the gust generator, is supported by comprehensive numerical studies. The wind tunnel model structure is designed, manufactured and equipped using our in-house aeroelastic model design process. The transfer functions of the actuators, required for the control design, are identified in a specific set-up on the model. The dynamic properties of the model structure are identified both wind-off in a standard ground vibration test (GVT), and wind-on at specific test points for identification. The paper focuses on the design and construction of the wing. Separate papers will give a specific view on design and analysis of the gust generator, as well as on the design

of the control laws, and an overview of the test matrix, the data acquisition systems and control hardware, and finally of the experimental results.

1 INTRODUCTION

Research towards reducing loads in primary structural aircraft components is an ongoing subject and has been so for many decades. Its main driver clearly is a reduction in aircraft weight and thus an increased transport capacity on the one hand, and an enhancement in fuel efficiency and ultimately environmental and economic aspects on the other hand. Two major branches of load reduction techniques can be identified: passive and active load reduction [1]. The latter typically refers to the use of control surfaces in order to influence lift and/or drag, also known as aeroservoelasticity. As this paper focuses on layout, design and manufacturing of the wind tunnel model, the reader is referred to the other corresponding works, which respectively detail the design of the gust generator, [2], the control law design, [3], and the project as whole, [4].

Load alleviation by passive means have been a subject of research for many years. In particular the identification of the manifold benefits attainable with composite materials has led to a considerable amount of research work in the past decades, starting in the late 70's with the work by Starnes Jr and Haftka [5], describing a weight minimization subject to combinations of buckling, strength, displacement and twist responses. The effect of bending torsion coupling [6], and non-symmetric laminates [7], were already investigated in the 80's, with a detailed overview of aeroelastic tailoring techniques in general provided by Shirk et al. [8]. Vanderplaats and Weisshaar provided an early overview on composite optimization techniques [9]. More recent aeroelastic tailoring works, including also the manufacturing aspects and constraints were given by Stodieck et al. [10–12] and Stanford et al. [13, 14], the latter one presenting an overview of the state-of-the-art.
In [15, 16] the author describes a composite stiffness optimization framework focusing on passive aeroelastic tailoring problems, a derivative of which was employed in the present work. It has already been applied in the layout of several wind tunnel models, among which for example the design of an aeroservoelastic model for a subsonic wind tunnel test, [17], or the design of a transonic model aiming at passive gust load alleviation, [18].

The paper at hand is organised as follows: Section 2 describes the model layout with a focus on the aerodynamic shape, Section 3 details the structural design with regard to finite element modeling, general constraints and requirements and the layup optimization. Section 4 addresses manufacturing and installation details, Section 5 provides a conclusion and outlook.

2 MODEL LAYOUT

Starting point for the aerodynamic layout was the *oLAF* baseline configuration, [19], Figure 1. In a first step it was scaled to feature a span of $1.6\,m$, measured from the end of the centre wing box to the wing tip. In addition to the main objective of active controllability, aim of the aerodynamic design was to achieve a suitable lift distribution for the targeted wing planform. The main design parameters are the airfoil and the spanwise twist distribution.

Due to its good-natured properties and the suitable thickness of 13%, the non-symmetrical airfoil *JD14*, already applied in the DLR project *Allegra*, [20], was also used for the *oLAF* model.

The consideration of trailing edge flaps and the resulting drag polars were investigated in *XFOIL*, Figure 2. The focus was on the *Reynolds* numbers prevailing in the mid and outer wing. Flow transition on the upper surface was let free, on the lower side the transition was set

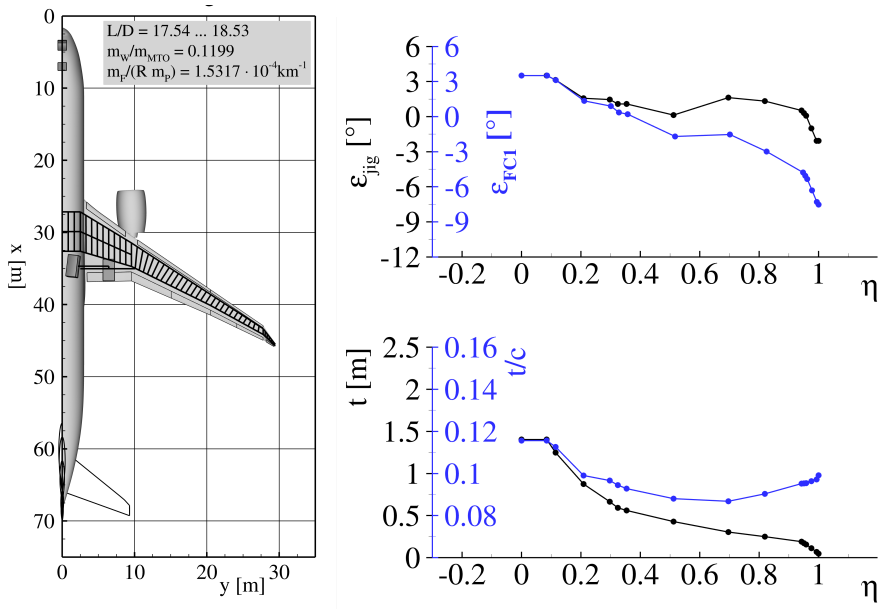

Figure 1: *oLAF* baseline configuration

to a position 2% in front of the hinge line. The flap depth is 20%. The $C_l - \alpha$ curves show a linear increase in lift over a wide angle of attack range, independent of the flap deflection investigated. According to the calculations, the stall behaviour is good-natured, although the maximum lift range in a 2D *XFOIL* calculation should always be viewed with reservation.

Initial calculations with an inviscid, incompressible 3D panel method showed that due to leading edge sweep and the relatively strong taper of the main wing, a very large positive twist of $3°$ towards the tip is necessary, in order to obtain a drag-minimised (almost) elliptical lift distribution. The positive twist in turn leads to an unfavourable lift coefficient distribution C_l, constantly increasing towards the tip and leading to flow separation and lift drop in the outer wing.

While the real wing in cruise flight achieves a rather elliptical lift distribution at high *Mach* numbers and a very large negative twist towards the tip, right plot in Figure 1, this does not seem to be possible in the incompressible case.

Since the lift coefficients required to achieve an optimum lift distribution for a given chord distribution are fixed, an alternatively introduced airfoil camber increase in the spanwise direction (in place of a twist increase) does not lead to an improved C_l distribution. For this reason, the objective of minimising induced drag was relaxed and replaced by a more favorable spanwise C_l distribution at the design point:

- ”design point”: a target lift coefficient of $C_L \approx 0.5$ at $1.0\,g$ cruise flight
- ”good-natured”: a local lift coefficient C_l not increasing towards the tip

The result is shown in Figure 3, left plot. For a total lift coefficient of $C_L = 0.47$, the resulting C_l, lower plot, shows constant values in the main wing and a slight decrease towards the tip. This is favorable in order to create a reserve for additional positive flap deflections in the outer wing without premature flow separation. The required design point twist distribution is shown in Figure 3, right plot. It represents the ”target twist” for the design point, which should be achieved under aeroelastic loads.

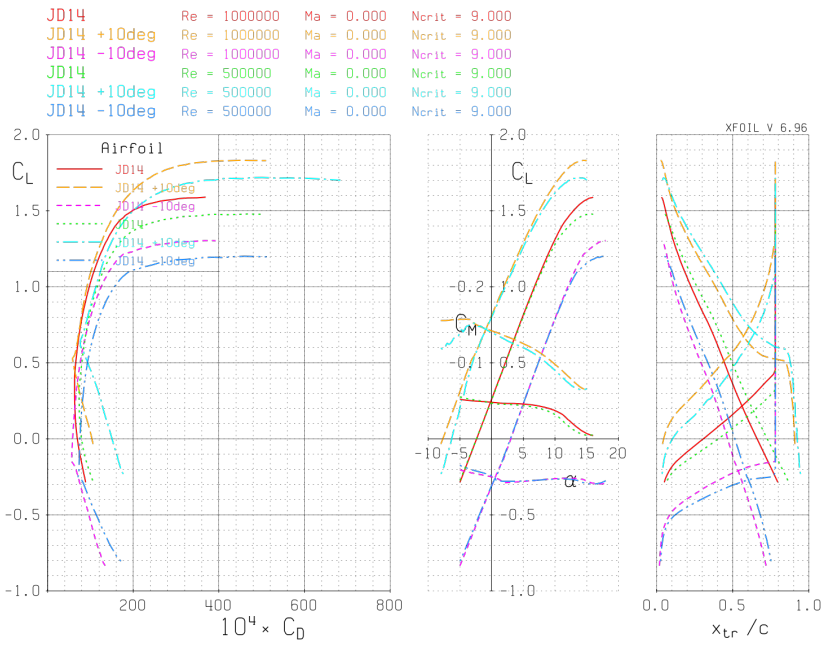

Figure 2: *JD14* 2D polars for various *Reynolds* numbers and flap deflections

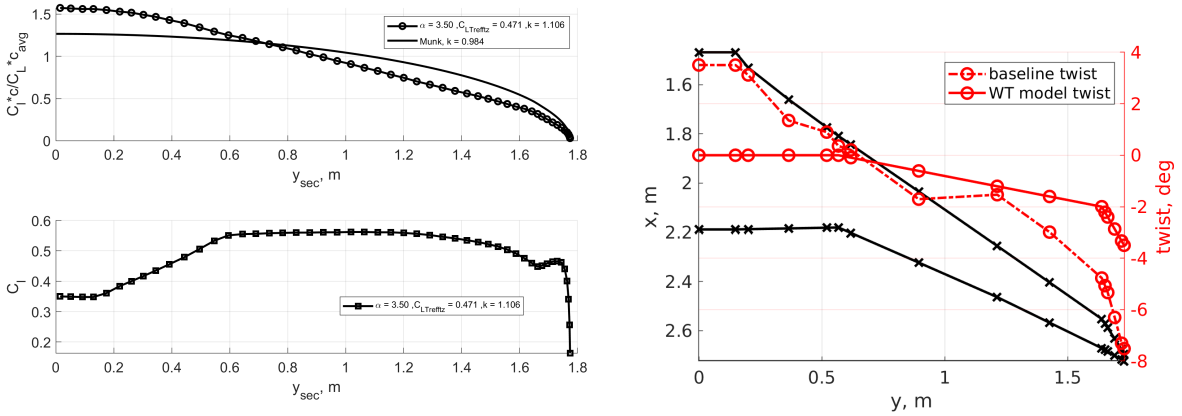

Figure 3: Global and local lift distribution (left plot) for target twist distribution (right plot)

The five flap and two spoiler positions were determined based on the baseline flap and spoiler concept, for the wind tunnel model featuring a constant relative flap depth of 20%. The general wing geometry with flap and spoiler locations, as well as the sensor positions, are summarized in Figure 4.

3 STRUCTURAL DESIGN

Experience gained in previous wind tunnel campaigns, e.g. [17] and [20], led to the decision of building the wing with load carrying wing skins and a foam core to support the skins and prevent buckling. The following sections describe the analysis model used in the structural design and the optimization of a suitable stacking sequence along the requirements and constraints.

3.1 Analysis Model

The *Nastran* finite element (FE) model, used for the computation of all structural and aeroelastic responses to be considered, is generated using the DLR in-house parametric modeling software

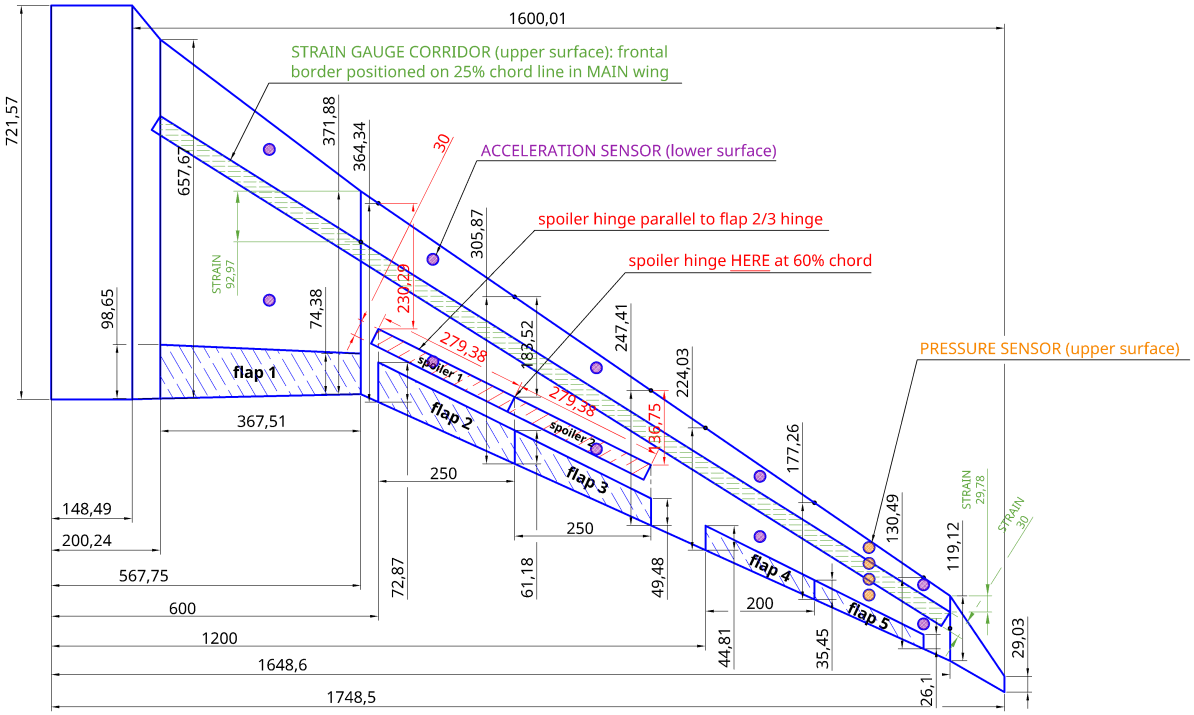

Figure 4: Wing geometry and sensor positioning

ModGen [21]. A representation of the FE model is shown in Figure 5, left wing. It comprises load carrying wing skins, extending from leading to trailing edge, rather than the usual box design as seen on full-scale aircraft. The skins are supported by a foam core to prevent it from buckling under compressional loads. While the skins are represented by shell elements in the FE model, the foam is modeled by volumetric elements. The aerodynamics are represented by a doublet lattice model (DLM) including a camber and twist correction, available in *Nastran* via the so-called W2GJ correction matrix, [22]. Coupling between the structural and the aerodynamic model is achieved by a dedicated set of coupling nodes, Figure 5, right wing. To this end, ribs connecting directly to the wing skins are introduced in nearly equidistant positions along the span. This technique is required by the *ModGen* modeling process, which necessitates the presence of a rib in order to generate coupling nodes. For the ribs to not add mass or stiffness, they are modeled without structural properties, as so-called dummy-ribs. Each outer node on a dummy-rib and thus wing skin is connected to an RBE3 interpolating element, the central, dependent node of which is placed in the quarter chord. Extending from the central node towards the leading and trailing edge are RBE2 rigid body elements, resulting in three nodes suitable for the aeroelastic coupling per dummy-rib. The entity of central nodes constitutes the so-called

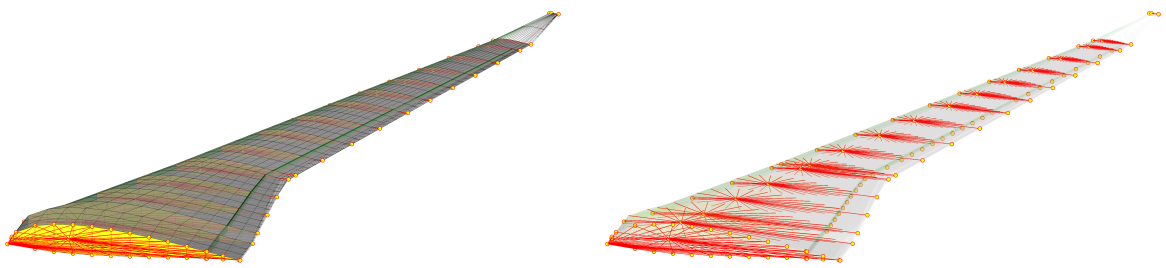

Figure 5: Finite element model (left) and coupling model (right)

load reference axis, which will also be addressed in the monitoring of deformation and twist responses. A detailed description of the coupling model can be found in [16]. Eventually, non-structural masses can be included as point masses, attached via rigid body elements.

3.2 Flap Modeling

For the wind tunnel model, the implementation of so-called fabric hinges was stipulated. This is realized by means of an aramid fabric along the hinge line on the lower surface, in addition to the regular stacking sequence. Once demolded, along the hinge line all plies except for the aramid layer will be cut and the aramid is used as a flexible hinge strip. This construction method is a proved and tested method for robust and backlash-free attachment of trailing edge flaps. In the finite element model a realistic implementation is achieved by modeling a slit in the upper surface wing skin and dedicated shell properties in the hinge area on the lower skin, Figure 6. The push rod to link actuator and flap in the real wing is represented by a beam element in the FE model.

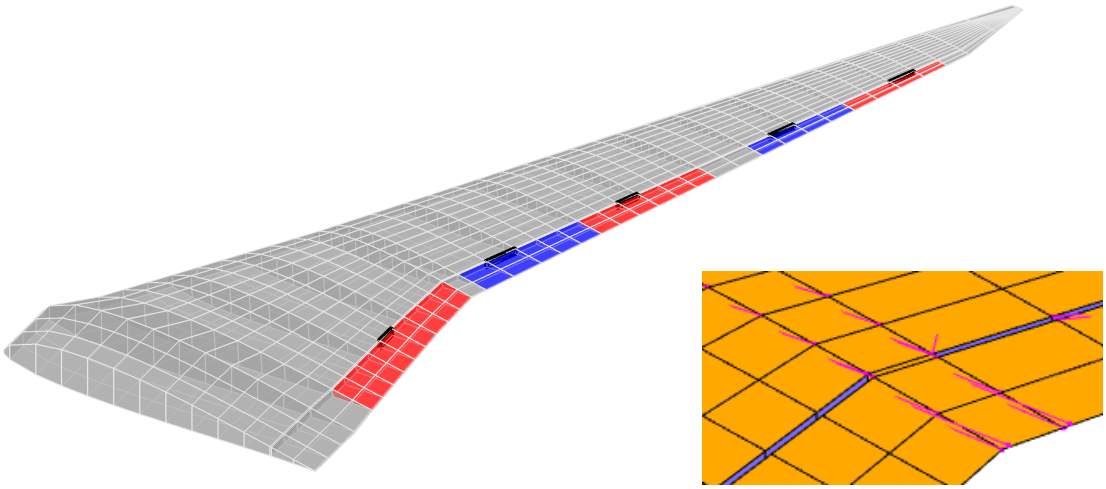

Figure 6: Flap modeling with fabric hinge

The implementation of the spoilers in the model is expected to have only a minor impact on the structural integrity, according to which its representation in the FE model was neglected.

3.3 Material, Load Cases, Constraints

Based on positive experiences regarding its material properties and processability, a unidirectional (UD) glass fiber with a dry areal weight of $220\,g/m^2$ and 93% fiber content in the warp direction (7% in the weft direction) was applied in the wing skins. The base fiber is E-Glas Silenka, with an E-modulus of $74\,GPa$, which along with an Epoxy resin and a fiber volume fraction of $fvf = 0.575$ results in the single ply material properties shown in Table 1. The fiber volume fraction was determined in previous test campaigns, [17], [20], for the same fiber, resin and hand layup technique, and thus also applied in the present research. Due to the weft content in the UD fabric, a single ply is modelled in the FE model using two individual plies with $90°$ rotated fiber angles. Properties of the *XPS 300* foam core are listed in Table 2.

Table 3 lists the analysed load cases. Load case LC1003 is the ”ultimate load case” at maximum wind speed and high angle of attack, which should not occur in reality, but simulates a failure

Table 1: Single ply material properties

E_{11}	E_{22}	G_{12}	ν_{12}	ρ	ε_t	ε_c	γ_s
$41.76\,GPa$	$12.94\,GPa$	$4.96\,GPa$	0.2637	$1976.3\,kg/m^3$	3.3%	2.2%	2.2%

Table 2: Foam core properties

E	G_{12}	ν_{12}	ρ
$20\,MPa$	$7.1\,MPa$	0.4	$30\,kg/m^3$

case. It is used to determine the maximum loads and thus the maximum strains. Load case LC1007 is a trim load case for determining and optimising the cruise twist.

Table 3: Load case definition

case	type	α	V, m/s	load factor
1000	α_{fixed}	$0.0°$	50	–
1001	α_{fixed}	$5.0°$	50	–
1002	α_{fixed}	$10.0°$	50	–
1003	α_{fixed}	$15.0°$	50	–
1004	α_{fixed}	$-5.0°$	50	–
1005	α_{fixed}	$-10.0°$	50	–
1006	α_{fixed}	$-15.0°$	50	–
1007	trim: cruise $C_L = 0.5$	–	50	$1.0\,g$
1008	trim: maneuver	–	50	$2.5\,g$
2001	eigenfrequ.	–	–	–
2002	ail.eff.flap 1	–	–	–
2003	ail.eff.flap 2	–	–	–
2004	ail.eff.flap 3	–	–	–
2005	ail.eff.flap 4	–	–	–
2006	ail.eff.flap 5	–	–	–

The non-structural masses, included in the FE model as point masses, were identical for all load cases (details on the sensoring provided in Section 4.1):

- five flap and two spoiler actuators and cabling
- twelve accelerometers and cabling
- ten pressure sensors and cabling
- $100\,g$ point mass at the winglet foot, serving to reduce the first bending frequency

The constraints to be considered were

- a minimum fiber failure safety factor for the ultimate load case LC1003
- the aeroelastic twist distribution closely matching the target twist distribution depicted in Figure 3 at cruise conditions, LC1007
- first bending eigenfrequency $\leq 10\,Hz$

The actuator type alloted for flap actuation, see also Section 4.1, limited the first bending eigenfrequency to a maximum of $\approx 10\,Hz$, owing to its upper boundary in dynamic range. It was assumed a priori that the first eigenmode has the largest contribution in the system response to a gust excitation.

3.4 Layup Optimization

An optimization model can be derived from the FE model by defining design variables and model responses. They are applied in a two-step optimization process, where in the first step element stiffness matrices (membrane stiffness **A** and bending stiffness **D**) are optimized, followed by a stacking sequence optimization. A detailed description of the two-step aeroelastic optimization process can be found in [16] and its application to wind tunnel model designs in the previously mentioned sources [20] and [17]. Applied to the *oLAF* model, it has became apparent that a stacking optimization - typically done with the objective to minimise the wing's mass or root bending moment for specific load cases - is not necessary. This can be attributed on the one hand to the relatively low aerodynamic loads in the low-speed tunnel and the resulting small number of required composite plies, which in turn considerably limits the effectiveness of a detailed stiffness optimization, as already shown in [17]. On the other hand, the main focus of the test is load reduction by active means. A key input to controller design is the dynamic (i.e. stiffness- and mass-related) FE model representation, and thus the controller performance essentially depends on the accuracy of the simulation model. In order to reduce the risk of discrepancies between FE and real model via inaccuracies in manufacturing overly complex stacking sequences, a manual, parametric stacking sequence optimization is favored.

The stacking sequence optimization comprised the investigation of a large range of different ply combinations. The corresponding parameters were wing jig twist distribution, the angle of each respective ply, as well as the rotation of an entire stack. The latter one is equivalent to a variation of the $0°$ reference line, for which per default the leading edge in the mid wing was selected. Eventually, a stacking sequence consisting of four plies $[+45°/-30°/+45°/-45°]$ applied in both, upper an lower wing skin, was derived. It represents a suitable combination of low first natural bending frequency and fiber strains. Figure 7 depicts the spanwise deformation and twist of the load reference axis for three different load cases (LC1000, LC1003, LC1007). Also plotted are the "load-free" jig twist and the target cruise twist. By adjusting the jig twist in combination with the stacking sequence, a good match of the twist in cruise flight, orange line, can be achieved. In this case, the calculated deformation at the wing tip is $\approx 65\,mm$.

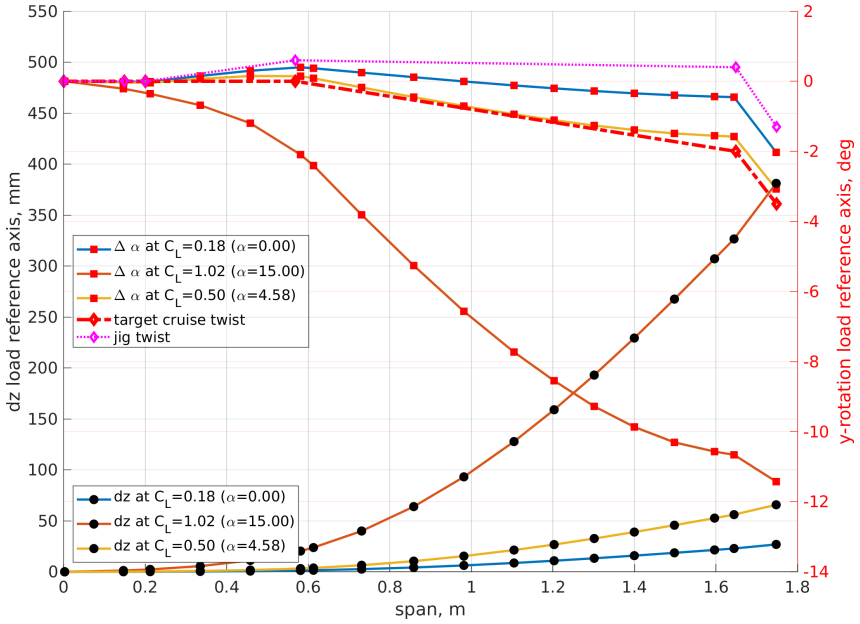

Figure 7: Spanwise deformation and twist distributions for various load cases

For the theoretical maximum load case with $90\,m/s$ and $15°$ angle of attack (red line), the deformation at the wing tip is $> 350\,mm$, with a tip twist of $\approx -11.5°$. An analysis of strains occurring for this load case shows that, taking into account a safety factor of 1.5 on the strain allowables listed in Table 1, a failure index *fi* of less than 1.0 is calculated, Figure 8, left plot. *Direction 1* depicts failure in fiber-direction. The failure index indicates the ratio of actual and allowable strain: $fi = \varepsilon_{real}/\varepsilon_{max}$.

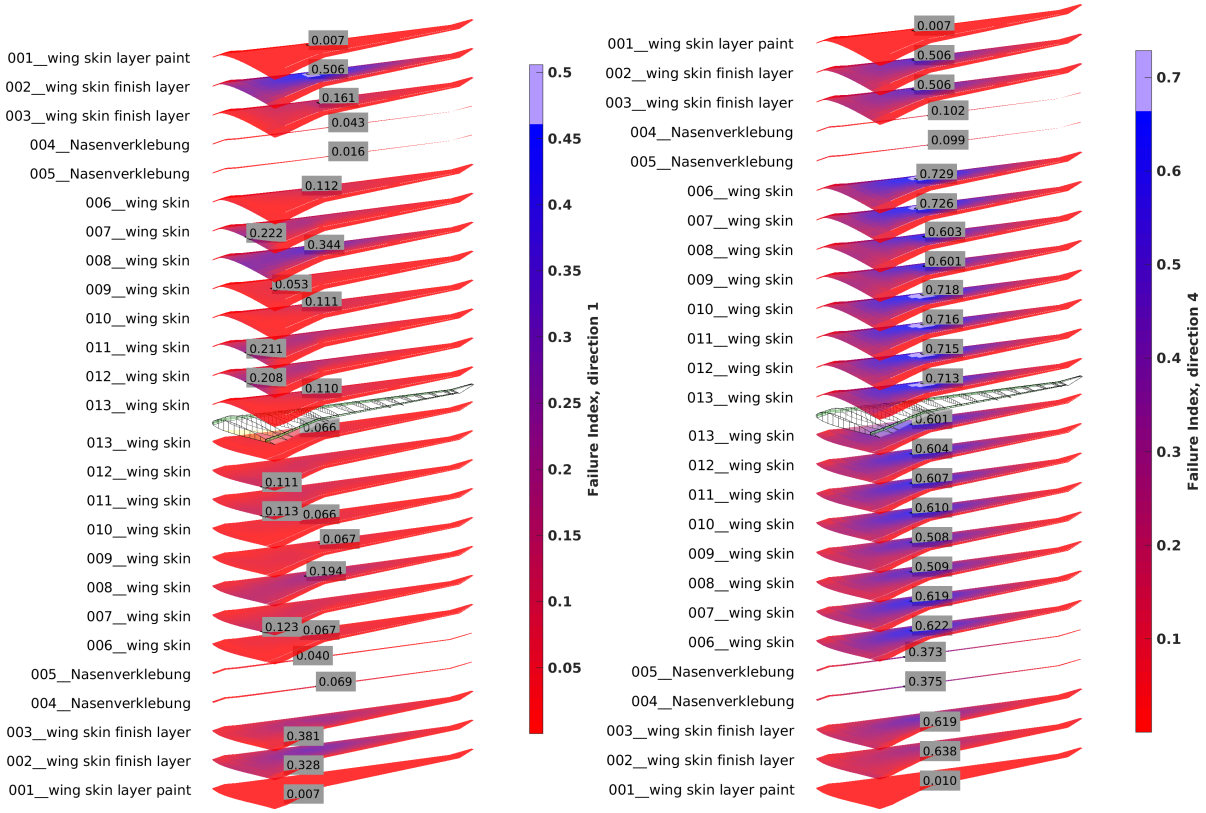

Figure 8: Failure indices in fiber direction (left) and overall (right)

Accordingly, values < 1.0 imply no fiber failure, while values > 1.0 indicate failure. Figure 8, right plot, shows the combined element-wise maximum of failure indices in the fiber direction (*Direction 1*), transverse to the fiber (*Direction 2*) and shear (*Direction 3*). Since each of the four UD plies is modeled as two individual plies as described above, eight plies are plotted per skin, with plies 006, 008, 010 and 012 in the upper skin representing the "main direction" (warp direction) of the UD ply. The maximum value is $fi = 0.73$. It should be noted once again that LC1003 is a freely selected design load case that could just as well have been defined with a $10°$ angle of attack instead of $15°$.

The most relevant eigenmodes with the consideration of a $100\,g$ tip mass (see Section 4.2) are plotted in Figure 9. As intended, the first bending eigenfrequency is well below $10\,Hz$.

4 MANUFACTURING

4.1 Actuation, Sensors and Mounting

The actuation of all movable surfaces was achieved with classical RC-type servos. Positive experience in terms of speed, strength and reliability was previously gained with the *MKS HBL990 HV* servo, [17], however, due to a height of $20\,mm$ it was not possible to fit them in the outer wing of the present model. Consequently, a comparably fast brushless digital servo *MKS HV93i HV* is chosen, whose thickness is only 12mm.

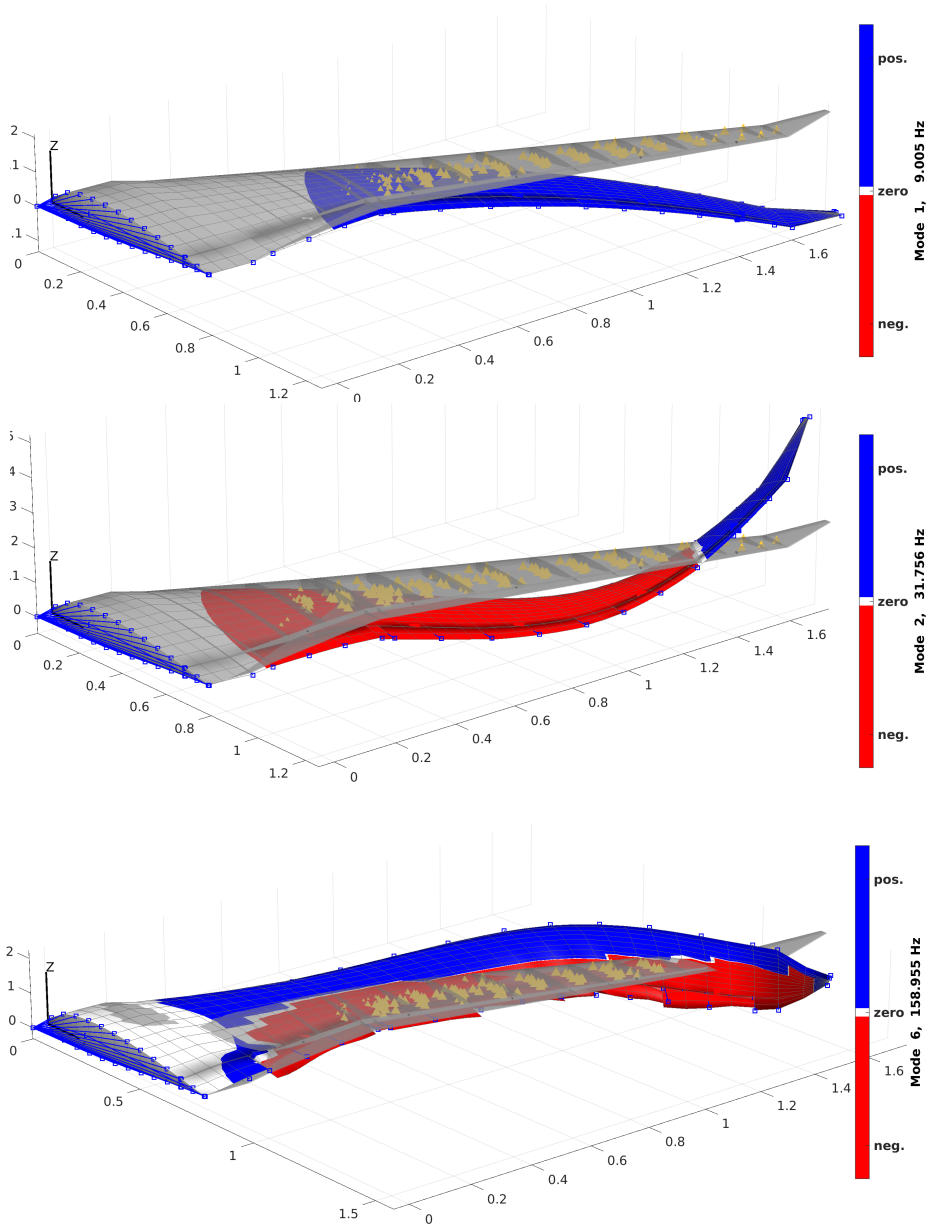

Figure 9: First bending, second bending and first torsion eigenmodes

The wing was equipped with *PCB 352C22/NC/ACS-97* accelerometers, distributed near the leading edge and the flap hinge line in five chordwise rows at $y = 400,\ 700,\ 1000,\ 1300,\ 1600\,mm$, resulting in ten sensor positions measuring in the z-direction (out-of-plane). Two additional sensors in the inner and outer wing were installed to capture the in-plane movement, eventually amounting to twelve accelerometers.

The accelerometers being mounted on the lower skin, similar positions for the pressure sensors were selected in the upper skin for the first three spanwise rows at $y = 400, 700, 1000\,mm$ and a fourth row at $y = 1500\,mm$ featuring four chordwise sensors. The sensor type was *Kulite XCQ-132-a-093-5D*.

A strain measurement fiber based on the *LUNA ODiSi-B* measurement system, [23], designed to read and process the optical strain data from the strain fiber embedded inside the wing, was installed in a spanwise corridor in the upper skin, featuring a purely spanwise alignment towards the tip and a $\pm 45°$ zig-zag orientation on the way back towards the root.

Eventually, the lower wing surface featured a lacquered point pattern (upper left picture in

Figure 13), serving as a basis for an image pattern correlation technique (IPCT) to measure three-dimensional surface deformations, [24].

The wing is mounted by means of an integrated root rib machined from aluminum, which is extruded $125\,mm$ into the wing's root and glued to its skins. It features an integral vertical plate outside the wing, specifically adapted to the piezo balance used to measure the three translational and three rotational forces and moments, see Figure 10.

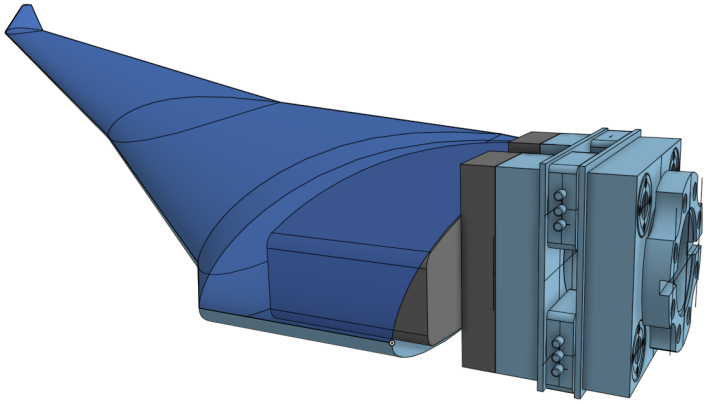

Figure 10: Aluminum root rib and piezo balance

4.2 Model Building

A graphical representation of the optimized stacking sequence, the so-called ply book, is shown in Figure 11. In combination with a stencil of $1:1$ scale and featuring the relevant fiber angles, Figure 12, the UD fabric plies are cut out.

Lamination of the wing skins was performed in a hand-layup technique (upper right picture in Figure 13) and vacuum bagging to guarantee optimal bonding and impregnation of the plies. The actuator and sensor installation required local cutouts and channels in the foam core in order to provide access to the wing skin laminates. While the accelerometers were glued onto 3D-printed platforms to guarantee accurate alignment with their intended measurement direction, the *Kulite* pressure sensors required the drilling of $0.6\,mm$ surface-perpendicular holes and a leak-free bonding to the wing skin. The servos were mounted in tailored frames, connecting to the flaps via rigid push rods in order to minimize free-play and flexibility (lower left picture in Figure 13). All cables were gathered and combined into channels leading towards the wing root, exiting the wing through a central hole in the root rib and piezo balance. At the winglet root, close to the wing tip, a ballast box was installed that could be loaded from the outside with metal weights of up to $350\,g$ depending on material type and size (lower right picture in Figure 13).

4.3 Identification and Update

While no dedicated modal identification of the model was performed, an examination of the first eigenfrequency with the help of the internal accelerometers, revealed a discrepancy between the finite element and the wind tunnel model, noting that the wind tunnel model was equipped with the largest possible additional tip mass of $350\,g$ from the beginning on. This was done in order to lower the bending frequency as much as possible and to increase actuator performance and controllability.

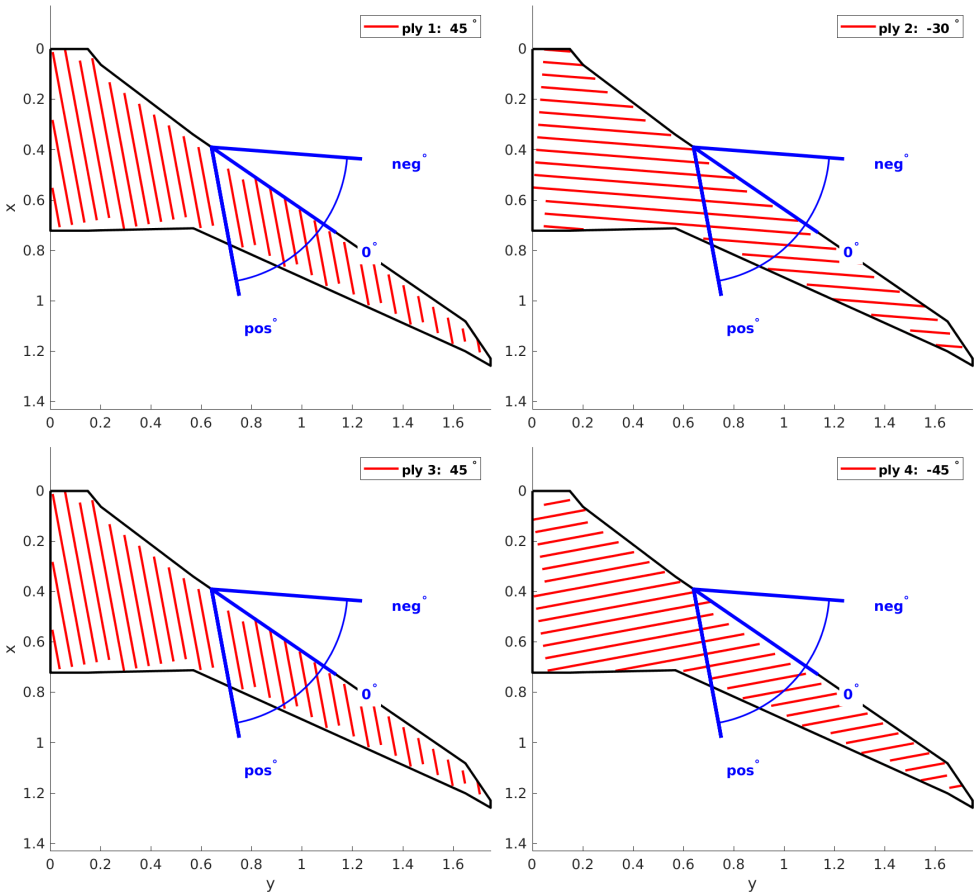

Figure 11: Ply book for upper and lower skin

Only physically meaningful model updates were made rather than arbitrary changes of stiffness and weight properties. Eventually, minor changes were required to achieve a good agreement between measured and computed eigenfrequency:

- update tip mass to $350\,g$
- update (reduce) accelerometer sensor and cable weight
- update (reduce) servo mount weight
- correct tip mass location
- adaption of the fiber angle of one ply by $5°$
- increase of fiber E-modulus by 7.5%
- model the staggered reinforcement layers in the clamping / aluminum rib root area

A first bending eigenfrequency of $\approx 8.5\,Hz$ was found from the measurement, which is also obtained in the updated model, see Figure 14.

5 CONCLUSION AND OUTLOOK

The complete process of designing, optimizing, building, and updating a wind tunnel model was presented in this paper. The wing layout is based upon basic dimensions and aerodynamic parameters that were developed according to the specific requirements and goals defined in the *oLAF* project. In order to evaluate the most promising combination of stacking sequence and jig twist distribution, various parameter studies were performed. Eventually, the wing was built and tested in the DNW-NWB subsonic wind tunnel in Braunschweig in February 2024. The experience gained with respect to model optimization, manufacturing aspects, in particular

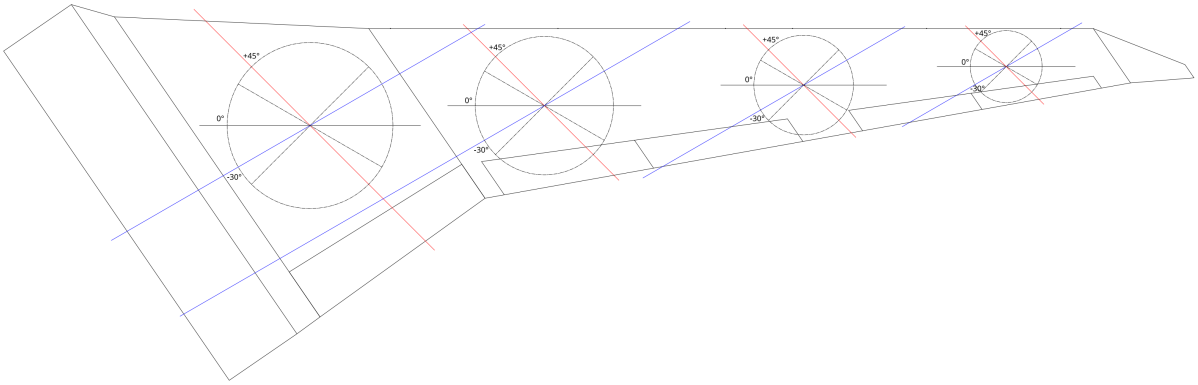

Figure 12: Ply stencil

Figure 13: Model building impressions

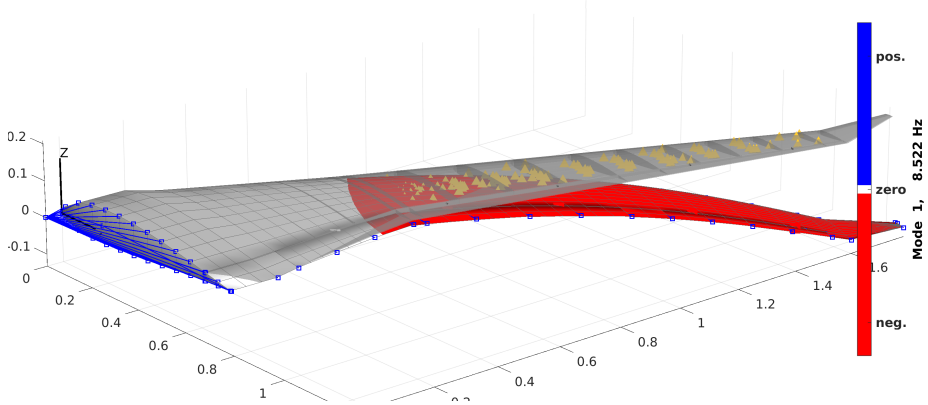

Figure 14: First bending eigenmod, updated model

concerning actuated flaps, but also regarding sensor installation and model mounting, will serve as a valuable input for future test campaigns, noting that the same lamination molds and thus aero geometry and clamping system will be used in the subsequent DLR project *SAFER*^{2}, which differs only in terms of its test objective.

ACKNOWLEDGEMENTS

The authors would like to acknowledge the support of Marc Braune, Holger Ernst, Markus Ritter, and Martin Tang from the DLR - Institute of Aeroelsticity, and Martin Weberschock for their valuable contributions to the realization and commissioning of the wind tunnel model.

6 REFERENCES

[1] Breuker, R. D. and Krüger, W. R. (2021). Passive loads alleviation through aeroelastic tailoring. *AIAA Scitech 2021 Forum*.

[2] Schmidt, T. G., Dillinger, J., Ritter, M., et al. (2024). Design and experimental characterization of a gust-generator concept with rotating-slotted cylinders in the low-speed wind tunnel dnw-nwb. *International Forum on Aeroelasticity and Structural Dynamics, IFASD 2024*.

[3] Stalla, F., Kier, T. M., Looye, G., et al. (2024). Wind tunnel testing active gust load alleviation of a flexible wing. *International Forum on Aeroelasticity and Structural Dynamics, IFASD 2024*.

[4] Krüger, W. R., Mai, H., Kier, T., et al. (2024). Assessment of active load control approaches for transport aircraft – simulation and wind tunnel test. *International Forum on Aeroelasticity and Structural Dynamics, IFASD 2024*.

[5] Jr, J. H. S. and Haftka, R. T. (1979). Preliminary design of composite wings for buckling, strength, and displacement constraints. *Journal of Aircraft*, 16, 564–570.

[6] Hollowell, S. J. and Dungundji, J. (1984). Aeroelastic flutter and divergence of stiffness coupled, graphite epoxy cantilevered plates. *Journal of Aircraft*, 21, 69–76. ISSN 0021-8669. doi:10.2514/3.48224.

[7] Green, J. A. (1987). Aeroelastic tailoring of aft-swept high-aspect-ratio composite wings. *Journal of Aircraft*, 24, 812–819.

[8] Shirk, M. H., Hertz, T. J., and Weisshaar, T. A. (1986). Aeroelastic tailoring - theory, practice, and promise. *Journal of Aircraft*, 23, 6–18.

[9] Vanderplaats, G. N. and Weisshaar, T. A. (1989). Optimum design of composite structures. *International Journal for Numerical Methods in Engineering*, 27, 437–448. doi:10.1002/nme.1620270214.

[10] Stodieck, O., Cooper, J. E., Weaver, P. M., et al. (2013). Improved aeroelastic tailoring using tow-steered composites. *Composite Structures*, 106, 703–715. ISSN 0263-8223. doi:http://dx.doi.org/10.1016/j.compstruct.2013.07.023.

[11] Stodieck, O., Cooper, J. E., and Weaver, P. M. (2016). Interpretation of bending/torsion coupling for swept, nonhomogenous wings. *Journal of Aircraft*, 53. ISSN 0021-8669. doi:10.2514/1.C033186.

[12] Stodieck, O., Cooper, J. E., Weaver, P. M., et al. (2017). Aeroelastic tailoring of a representative wing box using tow-steered composites. *AIAA Journal*, 55. ISSN 0001-1452. doi:10.2514/1.J055364.

[13] Stanford, B. K., Jutte, C. V., and Coker, C. A. (2018). Aeroelastic sizing and layout design of a wingbox through nested optimization. *AIAA Journal*, 1–10. ISSN 0001-1452. doi:10.2514/1.J057428.

[14] Jutte, C. and Stanford, B. K. (2014). Aeroelastic tailoring of transport aircraft wings: State-of-the-art and potential enabling technologies.

[15] Dillinger, J. K. S., Klimmek, T., Abdalla, M. M., et al. (2013). Stiffness optimization of composite wings with aeroelastic constraints. *Journal of Aircraft*, 50, 1159–1168. doi: 10.2514/1.C032084. Doi: 10.2514/1.C032084.

[16] Dillinger, J. (2014). *Static Aeroelastic Optimization of Composite Wings with Variable Stiffness Laminates*. TU Delft, Delft University of Technology. ISBN isbn:9789462035898. doi:10.4233/uuid:20484651-fd5d-49f2-9c56-355bc680f2b7.

[17] Dillinger, J. K. S., Meddaikar, Y. M., Lübker, J., et al. (2020). Design and optimization of an aeroservoelastic wind tunnel model. *Fluids 2020, Vol. 5, Page 35*, 5, 35. doi: 10.3390/FLUIDS5010035.

[18] Dillinger, J., Meddaikar, Y. M., Lepage, A., et al. (2022). Structural optimization of an aeroelastic wind tunnel model for unsteady transonic testing. *CEAS Aeronautical Journal*. ISSN 1869-5590. doi:10.1007/s13272-022-00612-3.

[19] Wunderlich, T. (2021). *oLAF M-1.3: Konfiguration für LA-Demonstrationsmodell bereitgestellt*. DLR - Institute of Aerodynamics and Flow Technology.

[20] Meddaikar, M. Y., Dillinger, J., Ritter, M. R., et al. (2017). Optimization & testing of aeroelastically-tailored forward swept wings. *IFASD 2017 - International Forum on Aeroelasticity and Structural Dynamics*.

[21] Klimmek, T. (2009). Parameterization of topology and geometry for the multidisciplinary optimization of wing structures.

[22] Dillinger, J., Abdalla, M. M., Meddaikar, Y. M., et al. (2015). Static aeroelastic stiffness optimization of a forward swept composite wing with cfd corrected aero loads. *International Forum on Aeroelasticity and Structural Dynamics, IFASD 2015*.

[23] Govers, Y., Meddaikar, M. Y., and Sinha, K. (2018). Model validation of an aeroelastically-tailored forward swept wing using fibre-optical strain measurements. pp. 1403–1417.

[24] Kirmse, T., Maring, S., Schröder, A., et al. (2016). Image based fan blade deformation measurements on an airbus a320 v2500 engine in ground operation. pp. 1–8. AIAA 2016-0386.

COPYRIGHT STATEMENT